

Simulation of high-latitude hydrological processes
in the Torne-Kalix basin: PILPS Phase 2(e)
3: Equivalent model representation and sensitivity experiments

Laura C. Bowling^a, Dennis P. Lettenmaier^a, Bart Nijssen^{a,b}, Jan Polcher^c, Randal D. Koster^d and Dag Lohmann^e

^a*Department of Civil and Environmental Engineering, University of Washington, U.S.A.*

^b*Now at: Departments of Civil Engineering and Engineering Mechanics, Hydrology and Water Resources, University of Arizona, U.S.A.*

^c*Laboratoire de Météorologie Dynamique du CNRS, Gif-sur-Yvette, France*

^d*Hydrological Sciences Branch, Laboratory for Hydrospheric Processes, NASA/Goddard Space Flight Center, Greenbelt, Maryland*

^e*NCEP Environmental Modeling Center (NOAA/NWS), U.S.A.*

Abstract

The Project for Intercomparison of Land Surface Parameterization Schemes (PILPS) Phase 2(e) showed that in cold regions the annual runoff production in Land Surface Schemes (LSSs) is closely related to the maximum snow accumulation, which in turn is controlled in large part by winter sublimation. To help further explain the relationship between snow cover, turbulent exchanges and runoff production, a simple equivalent model (SEM) was devised to reproduce the seasonal and annual fluxes simulated by 13 LSSs that participated in PILPS Phase 2(e). The design of the SEM relates the annual partitioning of precipitation and energy in the LSSs to three primary parameters: snow albedo, effective aerodynamic resistance and evaporation efficiency. Isolation of each of the parameters showed that the annual runoff production was most sensitive to the aerodynamic resistance. The SEM was somewhat successful in reproducing the observed LSS response to a decrease in shortwave radiation and changes in wind speed forcings. SEM parameters derived from the reduced shortwave forcings suggested that increased winter stability suppressed turbulent heat fluxes over snow. Because winter sensible heat fluxes were largely negative, reductions in winter shortwave radiation imply an increase in annual average sensible heat.

Keywords – Arctic regions, modeling, hydrology, atmosphere

1. Introduction

The Project for Intercomparison of Land Surface Parameterization Schemes (PILPS) Phase 2(e) was designed to evaluate the ability of the current generation of land surface schemes (LSSs) used in numerical weather prediction and climate models to represent high-latitude processes. Twenty-one LSSs were tested using observed meteorological forcing data for 218 grid cells that represented the 58,000 km² Torne-Kalix River basin in northern Scandinavia at a spatial resolution of 1/4 latitude and longitude (Bowling et al., 2002). . The experimental design and summary experiment results are described in Bowling et al. (2002). Nijssen et al. (2002) compare the simulated results with observations, and explore the inter-model differences in surface temperature, net radiation and runoff production.

The analyses of Phase 2(e) results presented by Bowling et al. (2002) and Nijssen et al. (2002) show that among all the models, annual runoff production is closely related to the maximum snow accumulation, which in turn is controlled in large part by winter sublimation. Models that detain more of the snow meltwater either as surface water storage or in the soil column, tend to generate a more attenuated hydrograph, which better matches observations (Nijssen et al., 2002). However, the analyses in Bowling et al. (2002) and Nijssen et al. (2002) are unable to reveal conclusive explanations for differences among the models in partitioning of latent and sensible heat, surface temperatures, and the effect of stability corrections for turbulent heat exchange. In addition, the design of the Phase 2(e) experiments did not tightly control model parameters, which complicates isolation of the contribution of specific parameterizations to the disparity among simulated results. The intent of this paper is to explore the nature of these relationships.

Koster and Milly (1997) analyzed a portion of the models from the PILPS Phase 2(a) experiment and found that regardless of LSS complexity, they could obtain a reasonable estimate of the simulated water balances through the development of simple monthly water balance models. The parameters for the monthly models were derived from simulations by the individual LSSs. That is, the equivalent models were inferred from simulations by the underlying detailed models. These parameters were then used to evaluate the interactions between evaporation and runoff processes within and among the LSSs. Gedney et al. (2000) used a similar methodology to evaluate predicted changes in surface hydrology as a result of climate change. In their experiment, equivalent simple bucket models were inferred for four LSSs in three regions, for two different climate scenarios.

In this paper, we condense the PILPS 2(e) simulation results for each of the models into the calibration parameters of a set of simple equivalent models (SEMs), which in turn are used to stratify model properties. We expand on the analysis of Koster and Milly (1997) and Gedney et al. (2000) by using a simplified monthly model to evaluate the interaction between snow cover, evaporation, and runoff processes. Thirteen of the twenty-one models that participated in Phase 2(e) returned sufficient model output variables to be used in this analysis. The derivation of simplified characterizations of each of these LSS is summarized in Section 3 and Appendix A. The results of the SEMs as applied to the Torne-Kalix data sets are presented in Section 4. In Section 5, the SEMs are used to explore the results of an inadvertent reduced wind speed and shortwave radiation 'experiment' conducted as part of PILPS Phase 2(e).

2. Study Areas

Five sub-regions of the Torne-Kalix River basins were chosen for analysis, as illustrated in Figure 1. The sub-regions are each composed of four $1/4^\circ$ model grid cells and were selected to

have fairly homogeneous vegetation, as summarized in Table 1. Two of the grid cells are at high elevation, and do not contain overstory vegetation; the remaining three grid cells are predominantly wooded, with varying annual precipitation and surface water (e.g. lakes and wetlands) fractions. Four of the sub-regions correspond approximately with the location of gauged sub-basins, two of which were used in other aspects of the PILPS 2(e) experiment (Bowling et al. 2002).

Figure 2 shows the variation of the monthly mean evaporative fraction (ratio of monthly evaporation to total available energy, defined in Section 3) with soil wetness, for each of the five study regions. Individual models are not identified since the general performance of all models is of primary interest. Monthly values were further screened to include only months for which the average available energy exceeds an equivalent of 1 mm/day of evaporation and snow covered area is less than 50% for each model, typically June through September. The unitless soil wetness is defined as:

$$\mu = (w - w_{\text{wilt}}) / (w_{\text{tot}} - w_{\text{wilt}}) \quad (1)$$

where w is soil moisture, w_{wilt} is the wilting point and w_{tot} is the total soil moisture storage capacity. In contrast to our expectations for temperate climates, Figure 2 shows that in the majority of the cases the evaporative fraction does not increase with increasing soil water availability. Six of the models do show an increase in evaporative fraction with increasing soil wetness for at least one of the study regions. However, these six models do not consistently show an increase for the same study region. The remaining models demonstrate little change in evaporative fraction for increasing soil wetness. There is some tendency for the evaporative fraction to decrease with increasing soil wetness due to a slight increase in soil wetness

following a decrease in evaporation. This further confirms that the LSS evaporation is not limited by water availability in this low net-radiation environment.

Figure 2 also shows that the models occupy different equilibrium ranges of soil wetness for similar runoff rates, consistent with the findings of Koster and Milly (1997). In general, the range of soil wetness values does not change markedly among the five regions, although the highest simulated soil wetness values are observed for the region with the greatest annual precipitation (Region 2). This is also the region with the highest simulated runoff rates. In general, the maximum runoff rates simulated by the models differ more among regions than among models, with runoff rates decreasing with decreasing annual precipitation (and decreasing annual snow accumulation). Nijssen et al. (2002) have shown that the majority of simulated runoff is produced following snowmelt in May and June. Examination of the surface and subsurface runoff components returned by each LSS separately (not shown) indicates the same relationship with increasing runoff rates with increasing snow precipitation for both surface and subsurface flow. This suggests that for the majority of the models the bulk of the runoff is produced as quick response surface or subsurface 'stormflow' rather than soil moisture induced drainage, as is to be expected in a region where runoff is dominated by snowmelt, often over frozen soils (soil freezing is represented by all but one of the models).

3. Simple Equivalent Model Description

The procedure used closely follows the methods of Koster and Milly (1997) and Gedney et al. (2000), with the addition of an energy-balance snow model and explicit tracking of the snow-covered and snow-free fractions, as illustrated in Figure 3. The SEM, which combines the energy-balance snow model and a water balance evaporation and runoff calculation, performs energy balance calculations for the snow portion only, and includes three state variables, the

root zone soil moisture, total snow water equivalent (SWE), and snow radiative temperature. Forcings for the SEM included: a) daily snow and rain precipitation, specific humidity, air temperature and downwelling radiation from the Phase 2(e) forcing files, and b) monthly interception evaporation, available energy and snow-covered fraction from each LSS. The water balance equation is expressed as:

$$\Delta w/\Delta t + \Delta W_e/\Delta t = P_e - E_t - R \quad (2)$$

where w is the total soil moisture, W_e is the water equivalent of snow, P_e is the effective precipitation (rain plus melt minus intercepted evaporation), E_t is the total (from snow, vegetation and bare ground) evapotranspiration, and R is total runoff. No distinction is made between surface runoff and root zone drainage.

The energy balance of the snow pack is expressed as:

$$W_e \cdot \rho_i \cdot C_p \frac{\Delta T_s}{\Delta t} = SW(1 - \alpha) + (LW - \sigma T_s^4) - Q_h - Q_{le} \quad (3)$$

and
$$Q_{le} = \rho_a (q_{sat}(T_s) - q_{air}) / r_a; \quad (3a)$$

and
$$Q_h = \rho_a \cdot C_{p_{air}} (T_s - T_{air}) / r_a. \quad (3b)$$

where T_s is the snow radiative temperature. The heat capacity of the snow and air, C_p and $C_{p_{air}}$, respectively, the Stephan-Boltzmann constant, σ , as well as the density of air and ice (ρ_a and ρ_i), are specified constants. Daily average shortwave radiation (SW), longwave radiation (LW), specific humidity (q_{air}), and air temperature (T_{air}), are input forcings. The snow model requires two LSS-dependent parameters, the snow albedo (α) and the effective aerodynamic resistance (r_a), which are determined by an automatic calibration procedure as described below. Snow accumulates when precipitation falls at daily air temperatures less than $0^\circ C$ and monthly LSS snow fractions (F_s) exceed 0.01%. The latter restriction is a logistical

constraint since the SEM depends on the monthly average snow-covered fraction returned by each LSS, the SEM cannot accumulate snow when the LSS predicts a snow fraction near zero.

. Melt occurs when T_s exceeds $0^\circ C$.

Accounting for snow cover, the total evapotranspiration (including transpiration, sublimation from the snow pack and bare soil evaporation) is:

$$E_t = F_s * E_s + (1 - F_s) E_c \quad (4)$$

with

$$E_c = \beta_{ns} * A_e + E_o,$$

and

$$E_s = \lambda_s \cdot Q_{le} = \rho_a (q_{sat}(T_s) - q_{air}) \cdot \lambda_s / r_a.$$

Here, F_s is the monthly snow-covered fraction, E_s represents evaporation and sublimation from the snow pack and E_c includes vegetation transpiration and bare soil evaporation. The effective available energy A_e is defined by Gedney et al. (2000), as

$$A_e = (R_n - G - LE_i) / \lambda \quad (5)$$

where R_n , G , and LE_i are the net radiation, ground heat flux and the latent heat released from evaporation of intercepted precipitation, respectively, and λ is the latent heat of vaporization. The effective available energy was scaled to have the units of a water flux by dividing the energy flux by λ . The LSS-dependent parameter, β_{ns} , in equation 4, can be viewed as the (unitless) model average evaporation efficiency with respect to available energy. The intercept, E_o , is then the average quantity of evaporation which can be sustained by negative sensible heat alone.

One departure from the method of Gedney et al. (2000), is that total evapotranspiration from snow-free ground, E_c , is solely a function of the total available energy at the ground surface. That is, there is no dependence of evaporation on soil moisture. This simplification was justified by the preliminary analysis in Section 2, which indicated that evaporation was largely independent of soil wetness in the five selected sub-regions. In addition, preliminary

experiments with simple models that included a moisture-dependence in the estimation of snow-free evaporation yielded a slight decrease in the ability to estimate annual evaporation for some models.

Total runoff is calculated as a piecewise linear function of the root zone soil wetness, in a manner similar to the root-zone drainage calculation used by Koster and Milly (1997), as follows:

$$\begin{aligned} R(\mu) &= m_{R1}(\mu - \mu_{R1}) & \mu \leq \mu_{R2}; \\ R(\mu) &= m_{R2}(\mu - \mu_{R2}) + R(\mu_{R2}) & \mu > \mu_{R2}. \end{aligned} \quad (6)$$

where μ is the unitless soil wetness as defined by Eq. (1), m_{R1} , m_{R2} , μ_{R1} and μ_{R2} are prescribed constants, and R is runoff in mm/day. Since Eq. (6) is dependent on soil wetness alone, runoff is not tied directly to precipitation. This is a reasonable assumption given the seasonal effect of snow accumulation in this region, and the lack of runoff response to summer rain events (Nijssen et al., 2002). The parameter μ_{R1} is the soil wetness threshold at which runoff is initiated and μ_{R2} is the threshold for initiation of fast stormflow response. m_{R1} and m_{R2} are the runoff rates (in mm/day) per incremental change in soil wetness.

Snow-free evaporation and runoff are functions of the updated soil wetness, which makes the scheme implicit. The LSS-dependent parameters required for the functions defined by Eqs. (3) through (6) (α , r_a , M_{R1} , M_{R2} , μ_{R2} , E_o , and β_{ns}) are derived using objective curve-fitting procedures for each model, which are described in Appendix A. A monthly value for the snow albedo, α_i , is determined for each model for each month. For snow-free evaporation calculations, the available energy is based on the net radiation output from each LSS, so a snow-free albedo is not needed. Preliminary analysis indicated that the aerodynamic resistance must take on different values for stable and unstable conditions (e.g. see Figure A.1). A

threshold near-surface temperature gradient is determined for switching between the stable and unstable values. The effective aerodynamic resistance, r_a , is therefore represented by three parameters: r_{a_stable} , $r_{a_unstable}$ and ΔT_{crit} , as described in Appendix A.

4. Application of the Simplified Model

A unique set of equivalent model parameters was estimated for each model, for each LSS for each of the five sub-regions, using forcing time series averaged over the four grid cells of each time series. The average parameters for all five sub-regions for each LSS are listed in Table 2. In order to evaluate the performance of the SEM, the parameter values for each LSS were used to integrate Eq. (2) over the ten year time period (1989-98). The ten-year simulation was performed twice consecutively to eliminate model initialization effects, with the second ten years of simulation used for the analysis.

The ability of the SEMs to represent the LSSs is summarized in Figure 4 for annual evaporation, soil wetness and SWE. The left-hand column shows the two regions with no overstory vegetation (Regions 1 and 2); the right-hand column shows the three regions with overstory vegetation (Regions 3, 4 and 5). The goodness-of-fit for soil wetness and evaporation are presented in terms of mean annual bias. SWE is presented as the cumulative distribution of the squared correlation coefficient of LSS and SEM SWE, for each region. For individual models, a higher r^2 represents a better fit, but the shape of the CDF yields information about the quality of fit for all models in a given region. It can be seen from the mean bias that the simple model is able to reproduce the simulated mean annual evaporation and soil wetness fairly well for most of the sub-regions. Evaporation appears to be better represented in areas without overstory, on average. The SEM fitted to the results of VISA (model M) performed poorly on evaporation, particularly in Region 4. VISA frequently had a positive near-surface temperature

gradient, which is apparently not well represented by the simple stability scheme. In the regions without overstory, ECMWF (model B) was not well represented. In this case, the fitting technique tended to overestimate r_a for the stable case, resulting in overestimation of sublimation in the spring. Bias in estimation of annual runoff (not shown) is similar to that for evaporation.

Somewhat surprisingly the seasonal cycle of SWE in general was better represented in regions with overstory, as shown by the cumulative probability distribution of the (r^2) between full models and the SEM in Figures 4e and 4f. In this figure the abscissa shows the cumulative probability, so that a curve that increases rapidly from zero suggests higher correlation among the SEM and full model simulations for a given region. Figure 5 shows the mean seasonal cycle of SWE from the LSSs and the simplified model for Regions 2 and 5. The figure shows that the simple model is able to capture the differences in seasonal snow both among regions and among models, despite errors in the fits. The simplified model both over and underpredicts maximum snow extent for different models, primarily due to sensitivity to the stability threshold (ΔT_{crit}) in the simplified model.

5. Characterizing the land surface schemes

5.1 Analysis of PILPS Phase 2(e) results

The simple water balance model developed in Section 3 has been shown to replicate simulated monthly and annual fluxes fairly well. We can now use the parameters of the simple models to investigate the partitioning of energy and precipitation in the LSSs. Because annual evaporation is represented without regard for simulated moisture content, the partitioning of precipitation in the SEM is controlled by three primary quantities: the effective aerodynamic resistance, snow albedo, and evaporation efficiency. The effective aerodynamic resistance is

controlled in turn by r_{a_stable} , $r_{a_unstable}$ and ΔT_{crit} . The aerodynamic resistance values found for each model, for each region are summarized in Figure 6. There is some tendency for higher resistances for the two regions without overstory vegetation, but the difference is not dramatic. ISBA (model D) and SEWAB (J) typically have much higher resistances in the stable case. These extremes have a limited effect on the differences in model performance, since turbulent fluxes are greatly suppressed for all models in the stable case. In the unstable case, CLASS (A), HY-SSiB (C), ISBA (D) and SEWAB (J) tend to have the highest resistances, with direct consequences for total snow accumulation, as shown in Figure 7. In Figure 7a, average annual total melt (a surrogate for maximum accumulation) is plotted versus the average effective aerodynamic resistance. Regions 2 and 5 are represented by different colors. Because Figure 7a shows the average r_a , it incorporates the effect of both r_a values, as well as ΔT_{crit} . Although CLASS does not have the highest resistances for Region 2, its effective resistance is the highest due to the relatively low value of ΔT_{crit} (-3.2 °C).

Figure 7b shows a similar figure for average snow albedo versus average annual total melt. Although the relationship between albedo and total snow accumulation is less well defined, there is still a noticeable effect in some cases. For example, NOAH (model H) and VISA (M) have similar effective resistances in Region 5, but large differences in melt. This difference is explained in part by the large difference in average albedo between the two models.

The influence of the evaporation efficiency is explored in Figure 8. This figure shows the mean annual evaporation efficiency versus annual available energy for Regions 2 and 5 for months with snow cover less than 10%. The vectors show the direction and magnitude of interannual variability (as represented by the standard deviation) of each of the quantities. The angle therefore indicates the relative influence of each quantity on the interannual variability of

summer evaporation from each model. For Region 2, these angles vary between 10° and 27° . For Region 5, the angles vary between 16° and 43° . This indicates that in all cases, the interannual variability in annual evaporation is explained in greater proportion by the changes in atmospheric forcings, rather than by differences in model parameterization.

Koster and Milly (1997) discuss model differences in terms of the average evaporation efficiency and the fraction of active soil moisture over which runoff occurs. They found that these quantities explain 94 percent of the intermodel variability in evaporation, thus clarifying that different evaporation rates in the LSSs resulted from different formulations of canopy interception and differences in the relative shape and position of the effective runoff and evaporation functions. For the Phase 2(e) results, our analysis indicates that in cold regions available energy rather than the soil moisture range controls intermodel differences in summer evaporation. As demonstrated by Nijssen et al. (2001), the intermodel difference in net radiation over the summer is equally attributable to differences in surface radiative temperature and land surface albedo.

To further explore the sensitivity of mean annual runoff to the aerodynamic resistance, albedo, snow cover fraction and evaporation efficiency, a sensitivity analysis was conducted in which each of these parameters was systematically fixed to the same value for all models for all years. In the case of snow cover fraction, the fixed value(s) were the average over all models of the monthly snow cover fractions. Snow albedo likewise was fixed at the average over all models, but was not changed seasonally. Figure 9a shows annual runoff for Region 2 predicted by each of the SEMs when snow cover fraction, albedo, resistances and evaporation parameters were fixed for all models and regions, listed in Table 3 (the 'fixed' case). There are still some differences in simulated runoff among models due to differences in runoff formulation.

However, these differences are small compared to the differences between the fixed case and the original runoff estimation using the simplified model (Figure 9b). Figures 9c – 9f show the percent difference between the perturbed run and the fixed run for the following perturbations: (1) fixed R_a 's and ΔT_{crit} , (2) fixed E_o , and β_{ns} , (3) fixed albedo and (4) fixed snow cover fraction. The percent difference is calculated as the difference between the perturbed case and the original simulation, normalized by the difference between the fixed case and the original simulation and multiplied by 100%. For Region 2, the difference between the fixed and original simulations is largely explained by the inter-model differences in effective aerodynamic resistance, and to a lesser extent by differences in evaporation efficiency. As shown in Figure 10, the situation is less clear for Region 5, which has overstory vegetation. In Region 5, aerodynamic resistance and evaporation efficiency still show the most sensitivity for most models, but the results are less consistent, and the differences in runoff formulations seem to play a larger role.

5.2 Sensitivity Analysis: results of the Phase 2(e) base run experiment

As indicated in Bowling et al. (2001), the original forcing data distributed to the participants had a low bias in shortwave radiation. The bias resulted from use of a general parameterization, based on the method of TVA (1972), to reduce radiation at the top of the atmosphere to clear sky radiation at the ground surface. A re-calculation of the shortwave forcing using the method of Eagleson (1970) with the turbidity factor estimated from station data in the PILPS 2(e) region, resulted in an average annual increase in shortwave radiation basin-wide of 36 percent. The revised data were distributed for a re-run experiment. The re-run data also included a corrected gridded wind field and hourly disaggregated precipitation. Correction of the error in the gridding of the wind speed dataset resulted in an increase in wind

speed of about 10 percent on average, with greater spatial variability than the shortwave radiation correction (in fact, although the domain average increased, some parts of the domain experienced an average decrease in wind speed). As discussed in Bowling et al. (2002), the disaggregation to hourly precipitation did not affect most of the models substantially.

Twenty of the LSSs involved in the Phase 2(e) experiment returned results for both the re-runs (higher shortwave) and the base runs (lower shortwave), thus leading to an interesting, if unplanned, sensitivity experiment. For simplicity of further discussion these are referred to as experiment (1) and experiment (2), respectively. All of the analysis presented so far has utilized the results of experiment (1). The primary result of the change between experiment (1) and (2) was a decrease in annual sensible heat flux for all of the models, as shown in Figure 11 for Region 2. Annual latent heat also decreased, but to a lesser extent. Snow pack evolution and runoff production showed little change.

The SEM is a useful tool to interpret the behavior of the LSSs as a result of changes in the wind speed and shortwave radiation. To incorporate both the effect of shortwave radiation and wind speed, which is not used in the SEM, the SEM parameters were re-estimated using the experiment (2) LSS results. The total available energy forcing for each of the simplified models was adjusted to reflect the experiment (2) forcing conditions, and the SEM simulations were repeated. The change in energy partitioning resulting from the SEM calculation is shown in Figure 12 for Region 2. Despite the simplicity of the model and the lack of a representation of energy components, the model was able to capture the magnitude and direction of the changes in Bowen ratio between experiment (1) and experiment (2), on average. However, there is a tendency for the SEM to underestimate the magnitude of the decrease in latent heat flux

between experiment (1) and (2), with a subsequent over-estimation of the change in sensible heat.

The coincidental change in both shortwave radiation and wind speed makes it difficult to interpret the results. However, changes in model performance during the winter months were due primarily to the change in the wind speed, because shortwave radiation in the Torne-Kalix basin is near-zero during the winter months. For Region 2, average wind speed increased between experiment (1) and (2), corresponding to a decrease of winter sensible heat for many models (Figure 13a). In Region 5, the average winter wind speed decreased by a similar magnitude, resulting in a consistent increase in winter sensible heat (decrease in magnitude) (Figure 13b).

Figure 14 shows the change in the fitted parameters when estimated with the reduced shortwave radiation and changed wind speed model runs for Regions 2 (black) and 5 (gray). For both regions, the critical temperature gradient for switching between stable and unstable conditions became more negative for experiment (2). Consequently, the average effective resistance for Region 2 decreased, despite both positive and negative changes in the individual resistances. The decreased resistance led to an enhancement of turbulent transfer of latent heat and a compensating increasingly negative sensible heat flux. For Region 5, both the stable and unstable resistances, and therefore, the effective resistance increased. This means that turbulent transfers were suppressed in experiment (2), leading to a decrease in the magnitude of the sensible heat flux, the opposite behavior to Region 2. Examination of the response of the other regions suggests that the Region 2 response is controlled by the change in wind speed and is little influenced by the presence or absence of overstory vegetation.

The average change in wind speed is near zero for Region 2 during the summer months, and modeled changes between experiment (1) and experiment (2) were primarily attributable to the decrease in shortwave radiation. Evaporation efficiency showed both positive and negative changes for Region 2 (Figure 14b). Because the evaporation efficiency is less than 0.5 for the majority of the models, most of the decrease in available energy is accounted for by a decrease in the sensible heat flux. In Region 5, the evaporation efficiency increased for nearly all models for experiment (2). The contrast with Region 2 suggests that the decrease in wind speed led to sensible heat consuming a smaller portion of available energy, and subsequently a smaller decrease in summer sensible heat.

6. Discussion and Conclusions

To explain the relationship among snow cover, turbulent exchanges and runoff production among the LSSs participating in the PILPS Phase 2(e) intercomparison, a simple equivalent model was devised to reproduce the seasonal and annual fluxes of 13 PILPS LSSs. This analysis shows that for the high-latitude Torne-Kalix River basin, the annual partitioning of precipitation and energy in the LSSs can be related to three primary parameters: snow albedo, effective aerodynamic resistance and evaporation efficiency. These parameters were estimated from LSS-simulated variables and used to parameterize the SEM for five regions within the Torne-Kalix River basin. On average, the SEM is better able to reproduce annual evaporation in areas without overstory vegetation (Regions 1 and 2). Because these areas are also the regions that receive the least annual radiation, this may be a reflection of a greater energy limitation on evaporation at these latitudes, in addition to vegetation controls. Over all models, the SEM is better able to represent the seasonal snow cycle in regions with overstory (Regions 3, 4 and 5), as measured using the squared correlation coefficient. This may be due in part to a

greater sensitivity to the aerodynamic resistance in Regions 1 and 2. The estimated aerodynamic resistance parameters tended to be higher for Regions 1 and 2, and annual runoff production is most sensitive to the aerodynamic resistance in these regions. In Regions 3, 4 and 5, annual runoff production is most influenced by both the effective aerodynamic resistance and the partitioning of energy into evaporation in the summer. Interannual variability in summertime evaporation is more influenced by interannual variation in model parameters in regions with overstory vegetation, than in regions without overstory. In all cases, however, interannual variation in available energy controls a larger proportion of the total variation in evaporation.

The SEMs were somewhat successful in reproducing the observed LSS response to a decrease in shortwave radiation forcings and changing wind speed. Fitted parameters to the revised forcings indicate that a larger proportion of available energy, and thus a decrease in available energy, is taken from sensible heat. Changes in wind speed can counteract this effect, leading to subsequent decreases in latent heat.

7. Acknowledgements:

This analysis could not have been completed with the efforts of the PILPS 2(e) participants who performed the simulations of the thirteen models presented here. These are: Douglas B. Clark, Mustapha El Maayar, Richard Essery, Sven Goers, Florence Habets, Bart van den Hurk, Jiming Jin, Daniel Kahan, Dag Lohmann, Sarith Mahanama, David Mocko, Olga Nasonova, Andrey B. Shmakin, Diana Verseghy, Pedro Viterbo, Youlang Xia, Xieyao Ma, Yongkang Xue, Zong-Liang Yang. In addition, we are indebted to the working group participants of the PILPS Phase 2(e) workshop held in Seattle, WA, who suggested this analysis approach.

8. References

Bowling, L.C., D. P. Lettenmaier, B. Nijssen, L. P. Graham, D. B. Clark, M. El Maayar, R. Essery, S. Goers, F. Habets, B. van den Hurk, J. Jin, D. Kahan, D. Lohmann, S. Mahanama, D. Mocko, O. Nasonova, P. Samuelsson, A. B. Shmakin, K. Takata, D. Verseghy, P. Viterbo, Y. Xia, X. Ma, Y. Xue, Z.L. Yang (2001), Simulation of high latitude hydrological processes in the Torne-Kalix basin: PILPS Phase 2(e), 1: Experiment description and summary intercomparisons, Global and Planetary Change, submitted.

Eagleson, P.S., 1970. *Dynamic Hydrology*. New York: McGraw-Hill.

Gedney, N., P.M. Cox, H. Douville, J. Polcher, and P.J. Valdes (2000), Characterizing GCM land surface schemes to understand their responses to climate change, *Journal of Climate*, 13, 3066-3079.

Koster, R.D. and P.C.D. Milly (1997), The interplay between transpiration and runoff formulations in land surface schemes used with atmospheric models, 10, 1578-1591.

Koster, R.D. and M.J. Suarez (1999), A simple framework for examining the interannual variability of land surface moisture fluxes, *Journal of Climate*, 12, 1911-1917.

Nijssen, B., L.C. Bowling, D.P. Lettenmaier, D.B. Clark, M. El Maayar, R. Essery, S. Goers, Y. Gusev, B. van den Hurk, J. Jin, D. Kahan, D. Lohmann, S. Mahanama, D. Mocko, O. Nasonova, P. Samuelsson, A.B. Shmakin, K. Takata, D. Verseghy, P. Viterbo, Y. Xia, X. Ma, Y. Xue and Z-L. Yang (2001), Simulation of high latitude hydrological processes in the Torne-Kalix basin: PILPS Phase 2(e), 2: Comparison of model results with observations, *Global and Planetary Change*, submitted.

TVA, 1972. Heat and mass transfer between a water surface and the atmosphere. *Water Resources Report No. 0-6803 14*. Tennessee Valley Authority.

Appendix A: Parameter estimation for the SEMs

Using the method of Koster and Milly (1997), μ_{R2} was found as the highest soil wetness for which the LSS produced monthly runoff less than 1 mm/day. The two parameters m_{R1} and m_{R2} were then found as the average slope of total runoff (surface and subsurface runoff returned from the LSSs) versus LSS soil wetness for the data series above and below this threshold, respectively. A sample of the fitted regression lines are shown in Figure A1 (a).

The parameters for snow-free evaporation were found by partitioning the monthly time series of available energy and evaporation into snow covered and snow-free periods. When the snow-covered fraction was less than 10 percent the entire grid cell was considered snow-free. The parameters β_{ns} and E_o were found by least squares regression of the LSS evaporation variables and available energy computed from the monthly net radiation, ground heat flux and

interception evaporation simulated by the LSS. A sample of the fitted regression lines are shown in Figure A1 (b).

The parameters of the snow model were derived using daily time series of the air temperature and surface pressure forcings and the surface temperature and sensible heat flux variables returned by each model for days on which the snow cover fraction as determined by each model exceeded 90%. Examination of plots of LSS simulated Qh versus $\rho_a \cdot Cp_{air}(T_s - T_{air})$, indicated that most models demonstrate two distinct modes of behavior, due to the utilization of corrections for the stability of the atmosphere, as shown in Figure A.1 (c). In order to segregate these two modes of behavior, the unstable aerodynamic resistance, r_{a_un} , was found as the slope of the least squares regression of Qh versus $\rho_a \cdot Cp_{air}(T_s - T_{air})$, for all days on which the bulk Richardson number was less than 0.0045. The critical temperature gradient, ΔT_{crit} , for switching between stable and unstable conditions was then found as:

$$\Delta T_{crit} = \frac{Q_h(98\%)}{\rho_a \cdot Cp_{air} \cdot r_{a_un}} \quad (A1)$$

where $Q_h(98\%)$ is the observed value of sensible heat flux that is exceeded on 98 percent of the days. The unstable aerodynamic resistance was found as the slope of the fitted line for all points for which $T_s - T_{air}$ is greater than the critical threshold.

Snow albedo, α , was calculated as the mean monthly value of snow albedo returned by each LSS, for each region. If a LSS did not return snow albedo, it was calculated as the mean land surface albedo returned by each model for months in which the snow cover fraction exceeded 75 percent. The value was held constant at the June value for months in which the snow cover fraction did not exceed 75 percent. Similarly, a time series of snow covered area was determined as the monthly average value returned by each LSS. If snow cover fraction was not

returned by a LSS, the fraction was specified as 0 or 1, depending on the presence or absence of snow.

Captions

Figure 1: Land cover map of the Torne-Kalix basin, showing the location of the five sub-regions used in the SEM analysis.

Figure 2: The dependence of runoff and summer evaporative fraction on scaled soil moisture for all models for each of the five sub-areas: a) monthly evaporative fraction for summer months and b) monthly runoff. To clarify the relationship, the dots are connected in order of decreasing evaporative fraction (increasing runoff), not in temporal order.

Figure 2: The dependence of runoff and summer evaporative fraction on scaled soil moisture for all models for each of the five sub-areas: a) monthly evaporative fraction for summer months and b) monthly runoff.

Figure 3: Simple Equivalent Model Schematic

Figure 4: Goodness of fit for the simple equivalent models versus the LSS simulations for a) and b) annual evaporation bias, c) and d) annual soil wetness bias and e) and f) squared correlation coefficient of monthly SWE. The left hand column shows Regions 1 and 2, and the right hand column shows Regions 3, 4 and 5, coded by number.

Figure 5. Mean monthly SWE LSS simulated (solid line) versus simple equivalent model estimate (dashed line), for Region 2 (black) and Region 5 (gray). Letters correspond to the LSS listed in Table 2.

Figure 6: Aerodynamic resistance parameters controlling turbulent fluxes from snow, for each region: a) stable case and b) unstable case.

Figure 7: Average annual melt predicted by each bucket model as a function of fitted parameters: a) average aerodynamic resistance and b) average snow albedo.

Figure 8: Average annual evaporation efficiency for no-snow condition, versus average annual available energy from the LSS: Region 2 (black) and Region 5 (gray). Arrows show magnitude of interannual variability (as represented by the standard deviation) for each quantity.

Figure 9: Sensitivity of annual runoff production to bucket model parameters for Region 2. a) Annual runoff with all parameters fixed, b) difference between original and fixed runoff, c) percent difference due to fixed R_a , d) percent difference due to fixed evaporation efficiency, e) percent difference due to fixed albedo and f) percent difference due to fixed snow cover fraction.

Figure 10: Sensitivity of annual runoff production to bucket model parameters for Region 5. a) Annual runoff with all parameters fixed, b) difference between original and fixed runoff, c) percent difference due to fixed R_a , d) percent difference due to fixed evaporation efficiency, e) percent difference due to fixed albedo and f) percent difference due to fixed snow cover fraction.

Figure 11: Magnitude and direction of change in average annual sensible and latent heat flux from the original LSSs for Region 2 going between experiment (1) and experiment (2).

Figure 12: Magnitude and direction of change in average annual sensible and latent heat flux from the SEM for Region 2 going between experiment (1) and experiment (2) forcings and parameters.

Figure 13: Mean monthly change (experiment 1 – experiment 2) in incoming shortwave (gray dashed), sensible heat (solid black) and wind speed (black dashed) for the LSSs: a) for Region 2 (no overstory) and b) for Region 5 (overstory).

Figure 14: Change in fitted parameters between experiment (1) and (2) for Region 2 (black) and Region 5 (gray): a) ΔT_{crit} , b) B_{ns} , c) r_{a_stable} and d) $r_{a_unstable}$

Figure A1: Sample fitting procedure for one LSS: a) Runoff, b) Evaporation and c) aerodynamic resistance.

Table 1: Description of modeling sub-regions

Group	Annual Precipitation (mm)	Percent Snow (%)	Annual Air Temperature (°C)	Mean Elevation (m)	Dominant Vegetation
1	703	48.4	-2.1	697	Open/closed shrubland
2	1273	55.1	-2.2	974	Open shrubland/ bare ground
3	612	43.1	-1.4	404	Wooded grassland
4	746	42.0	0.0	299	Woodland
5	710	38.5	0.9	126	Wooded grassland

Table 2: Average simple equivalent model parameters for each LSS

Model	Snow model			Evap			Runoff response			
	ΔT_{crit}	r_{a_st}	r_{a_un}	α	β_{ns}	E_o	M_{R1}	μ_{R2}	μ_{R1}	M_{R2}
A CLASS	-2.5	0.0013	0.0134	0.72	0.59	0.67	7.0	0.4	0.1	29.0
B ECMWF	-2.2	0.0034	0.0516	0.75	0.54	0.79	9.8	0.5	0.4	40.8
C HY-SSiB	-4.1	0.0020	0.0060	0.62	0.64	0.26	8.3	0.8	0.6	170.3
D ISBA	-3.1	0.0004	0.0172	0.80	0.58	0.64	5.1	0.4	0.2	102.3
E MECMWF	-2.8	0.0018	0.0211	0.83	0.57	0.78	10.5	0.8	0.6	66.0
F MOSES	-2.5	0.0057	0.0436	0.81	0.48	0.94	10.8	0.9	0.7	10.8
G MOSES-CEH	-2.6	0.0054	0.0437	0.81	0.42	0.91	15.6	0.8	0.7	25.9
H NOAH	-2.9	0.0106	0.0251	0.44	0.44	0.48	13.9	0.9	0.7	13.9
I SAST	-2.1	0.0056	0.0367	0.68	-0.06	1.47	18.8	0.6	0.5	94.5
J SEWAB	-9.2	0.0001	0.0079	0.82	0.48	0.48	9.6	0.8	0.7	159.3
K SWAP	-3.6	0.0029	0.0105	0.85	0.64	0.69	8.4	1.0	0.5	8.4
L VIC	-2.8	0.0019	0.0187	0.76	0.53	0.56	8.5	0.7	0.5	152.8
M VISA	-0.8	0.0091	0.0837	0.79	0.48	0.77	13.3	0.6	0.4	138.0

Table 3: Parameter values used for sensitivity runs

	ΔT_{crit}	r_{a_st}	r_{a_un}	α	β_{ns}	E_o
Constant in time:	-3.16° C	259 sm ⁻¹	34.3 sm ⁻¹	0.75	0.49	0.73 mm
Monthly varying snow-covered fraction:	0.99, 0.99, 0.99, 0.94, 0.60, 0.06, 0.00, 0.00, 0.07, 0.56, 0.91, 0.96					

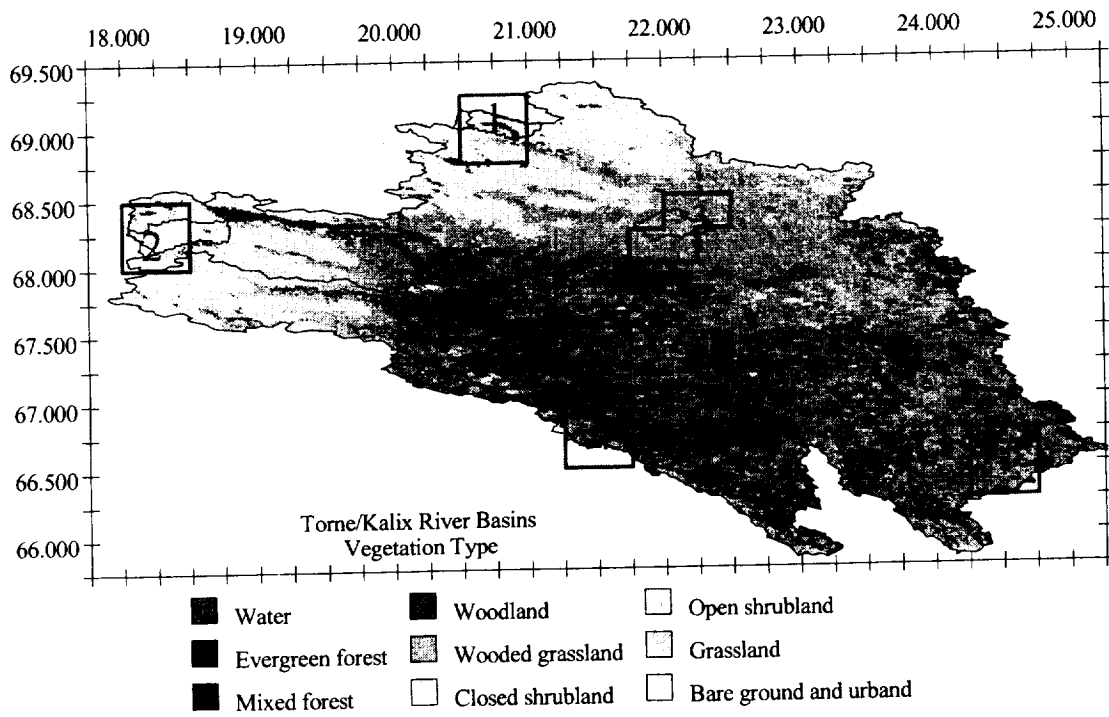


Figure 1: Land cover map of the Torne-Kalix basin, showing the location of the five sub-regions used in the simple model analysis.

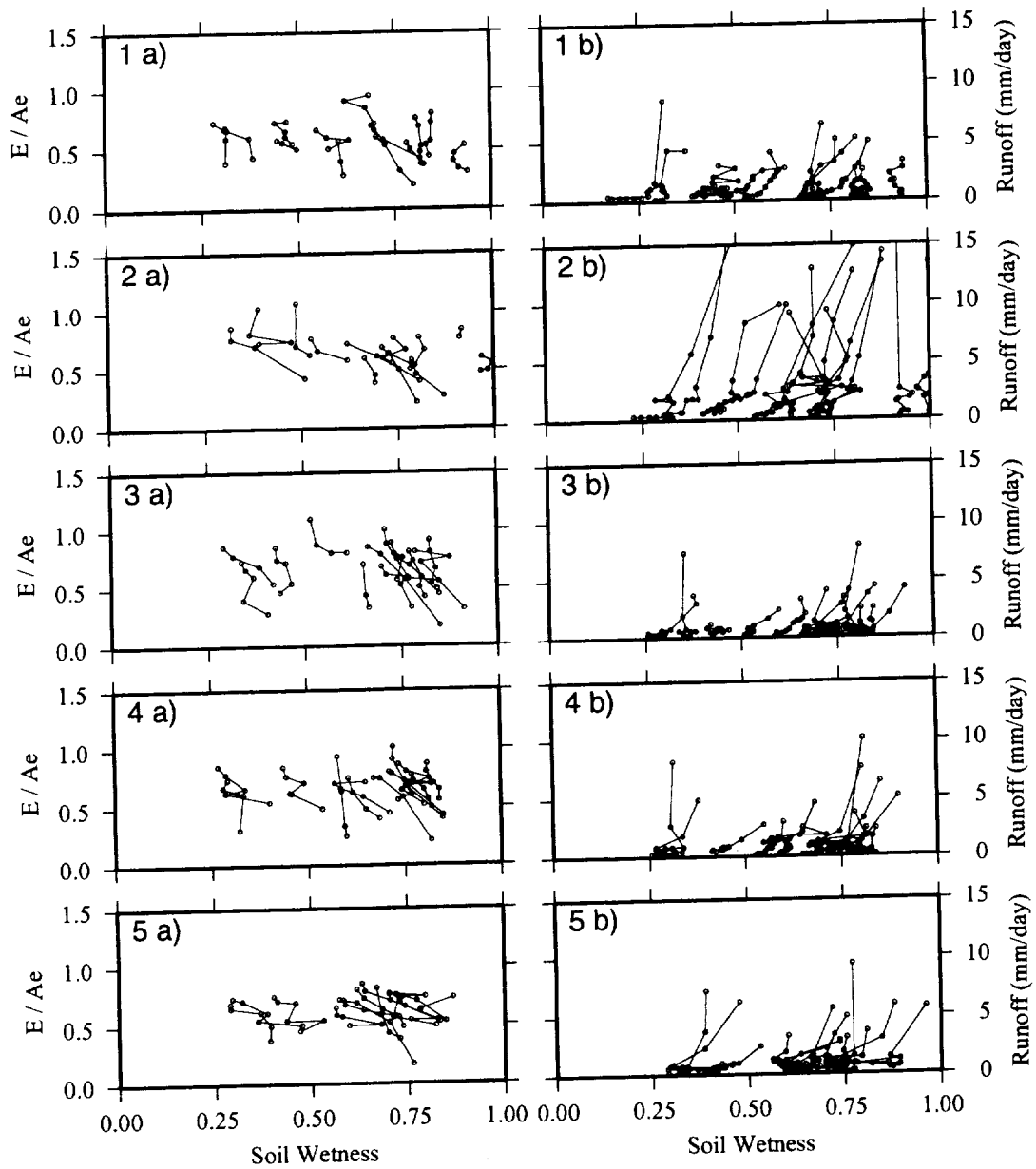


Figure 2: The dependence of runoff and summer evaporative fraction on scaled soil moisture for all models for each of the five sub-areas: a) monthly evaporative fraction for summer months and b) monthly runoff. To clarify the relationship, the dots are connected in order of decreasing evaporative fraction (increasing runoff), not in temporal order.

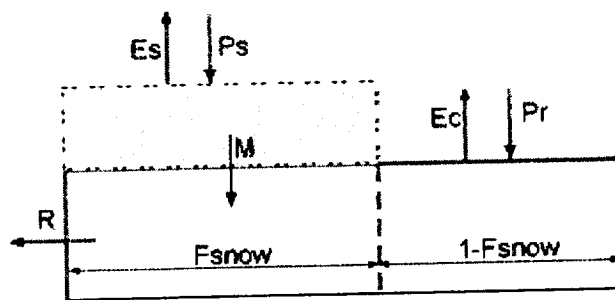


Figure 3: Bucket Model Schematic

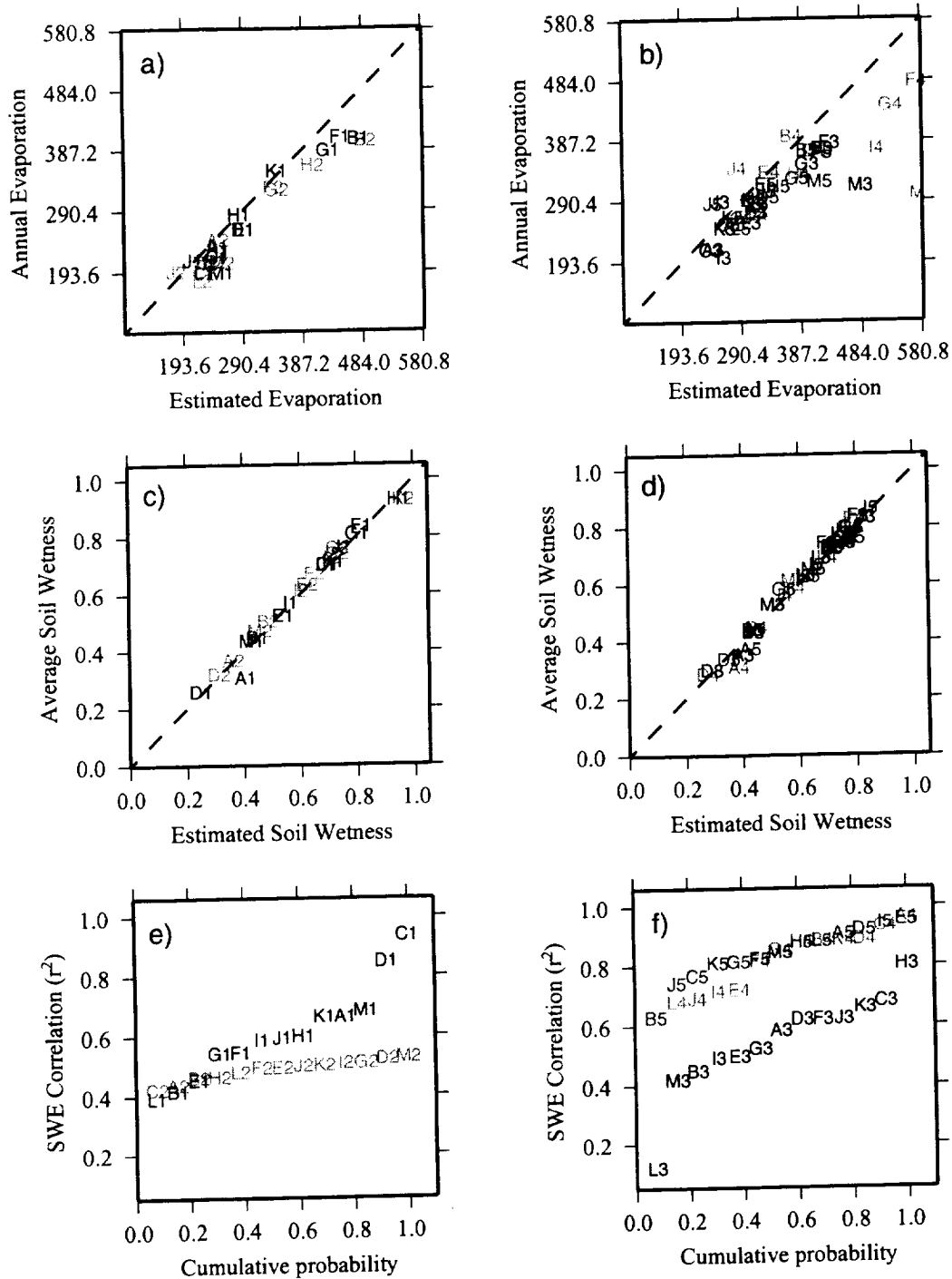


Figure 4: Goodness of fit for the simple bucket models versus the LSS simulations for a) and b) annual evaporation bias, c) and d) annual soil wetness bias and e) and f) squared correlation coefficient of monthly SWE. The left hand column shows Regions 1 and 2, and the right hand column shows Regions 3, 4 and 5, coded by number.

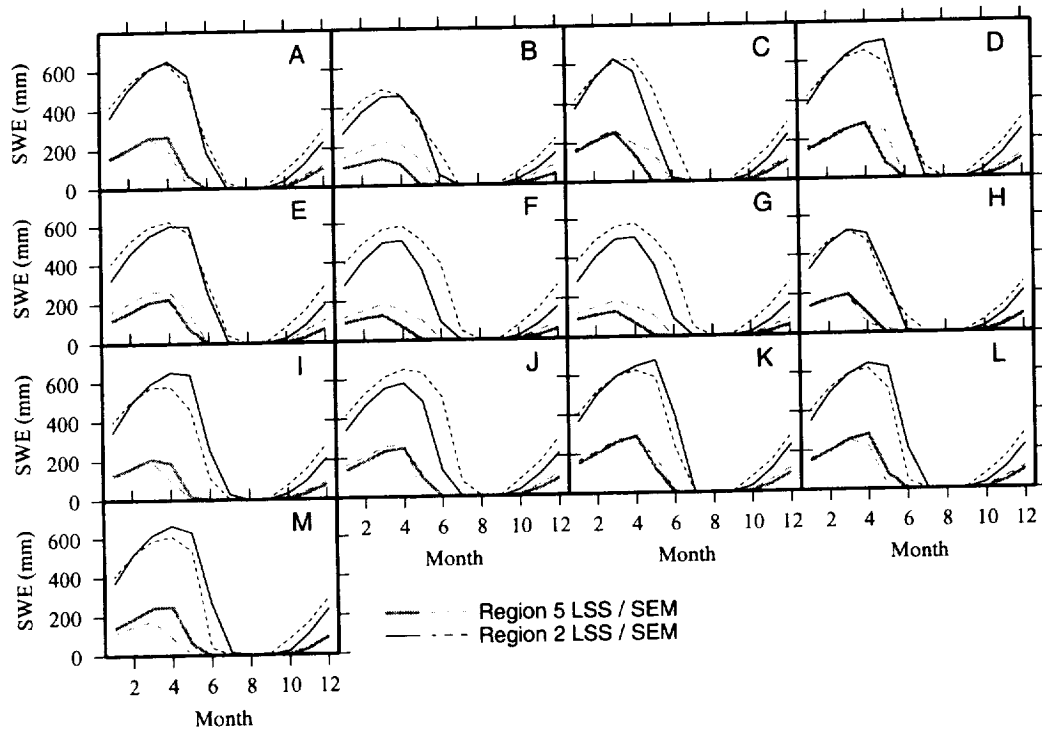


Figure 5. Mean monthly SWE LSS simulated (solid line) versus bucket model estimate (dashed line), for Region 2 (black) and Region 5 (gray). Letters correspond to the LSS listed in Table 2.

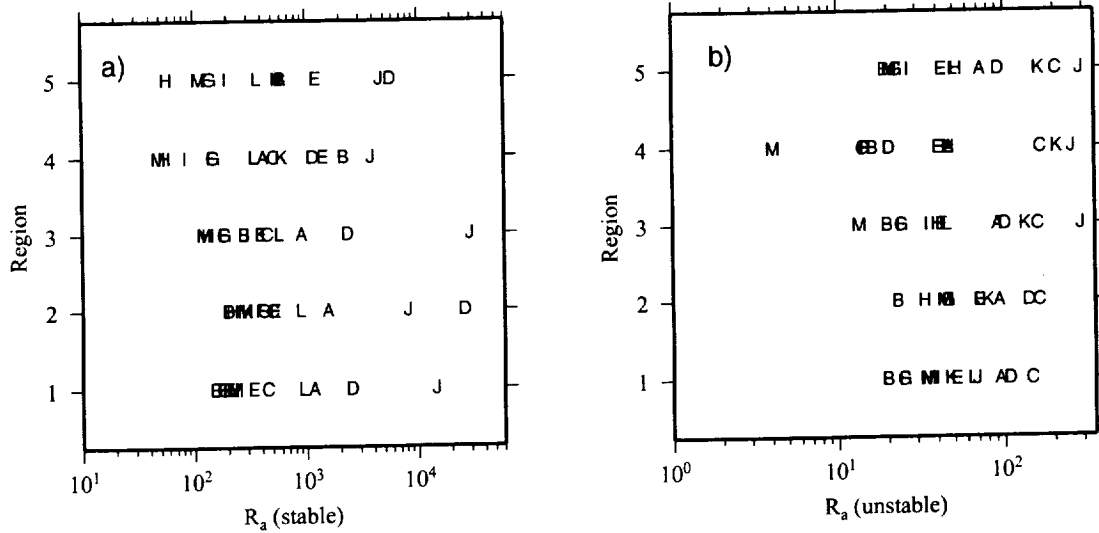


Figure 6: Aerodynamic resistance parameters controlling turbulent fluxes from snow, for each region: a) stable case and b) unstable case.

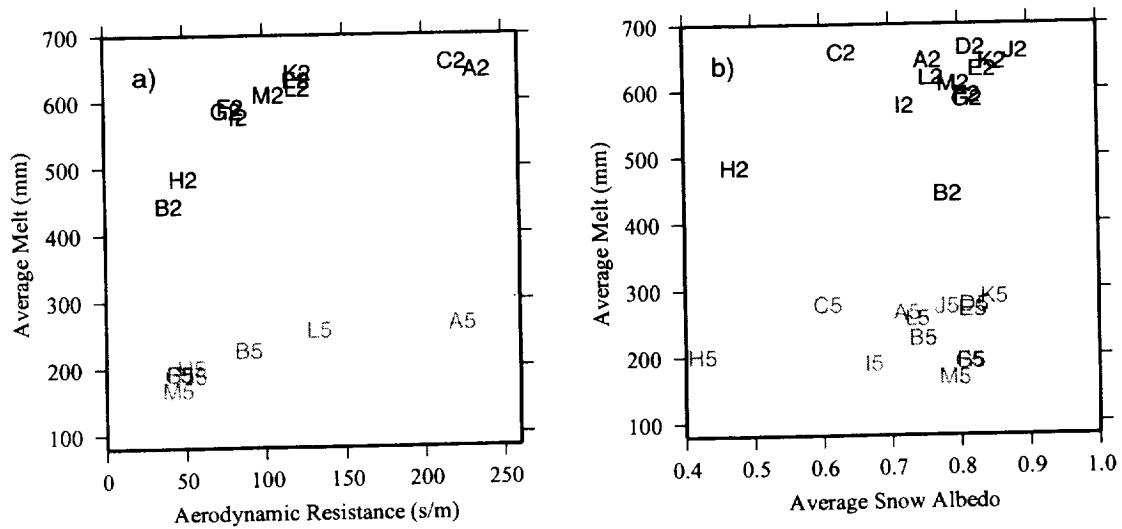


Figure 7: Average annual melt predicted by each bucket model as a function of fitted parameters: a) average aerodynamic resistance and b) average snow albedo.

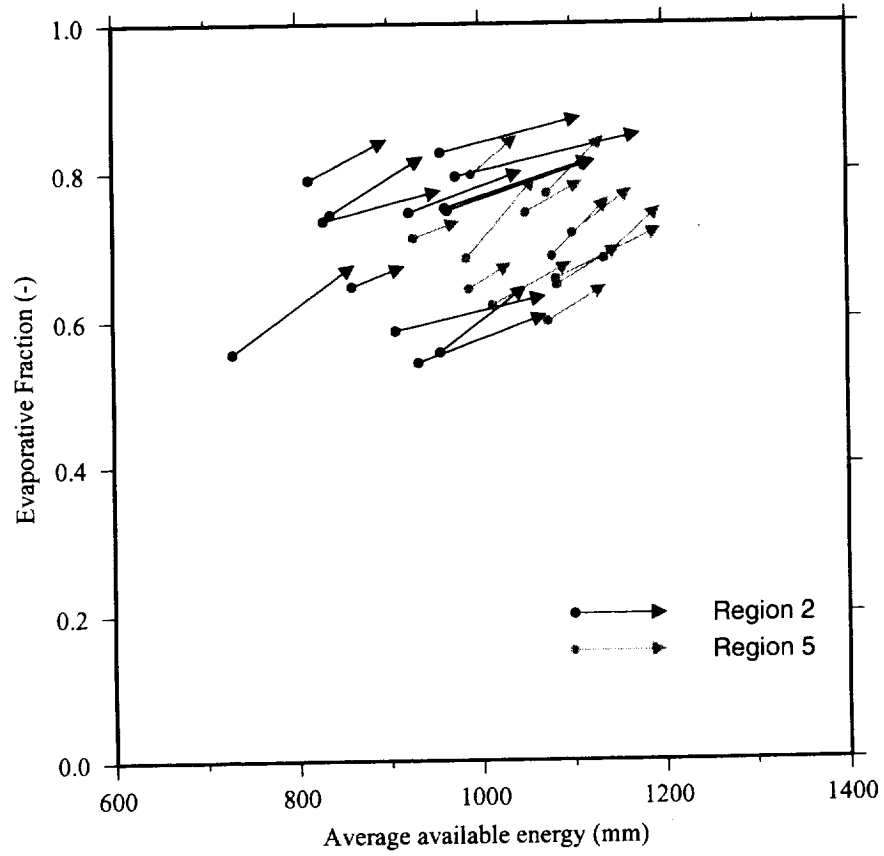


Figure 8: Average annual evaporation efficiency for no-snow condition, versus average annual available energy from the LSS: Region 2 (black) and Region 5 (gray). Arrows show magnitude of interannual variability (as represented by the standard deviation) for each quantity.

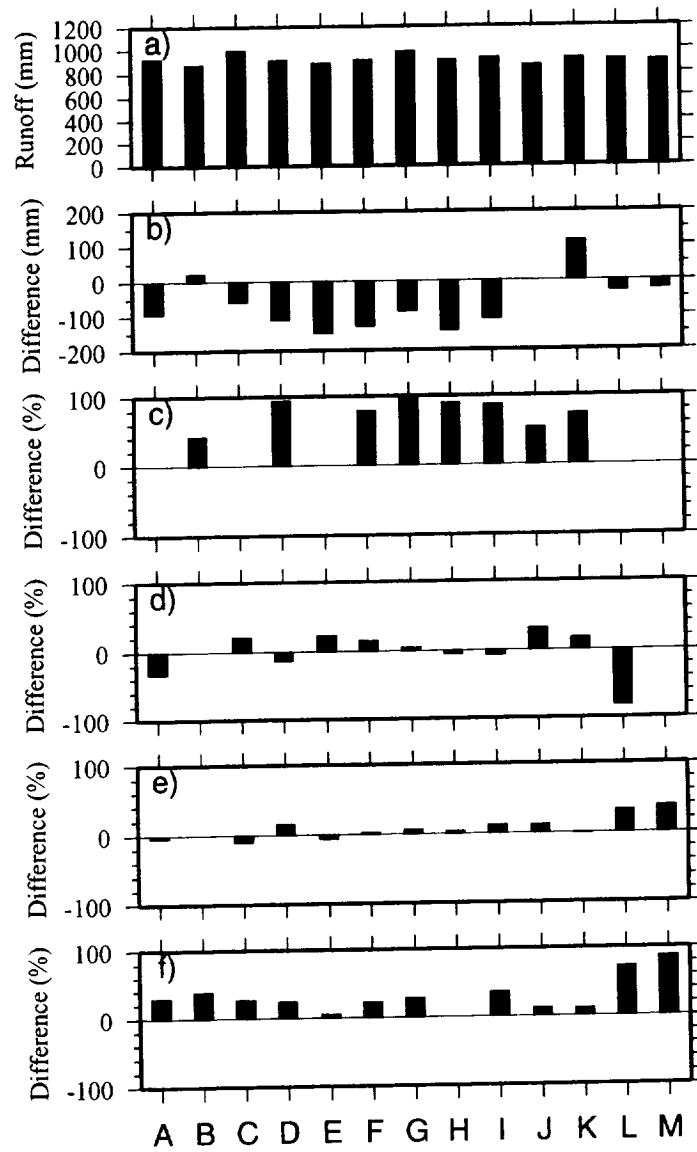


Figure 9: Sensitivity of annual runoff production to bucket model parameters for Region 1. a) Annual runoff with all parameters fixed, b) difference between original and fixed runoff, c) percent difference due to fixed R_a , d) percent difference due to fixed evaporation efficiency, e) percent difference due to fixed albedo and f) percent difference due to fixed snow cover fraction.

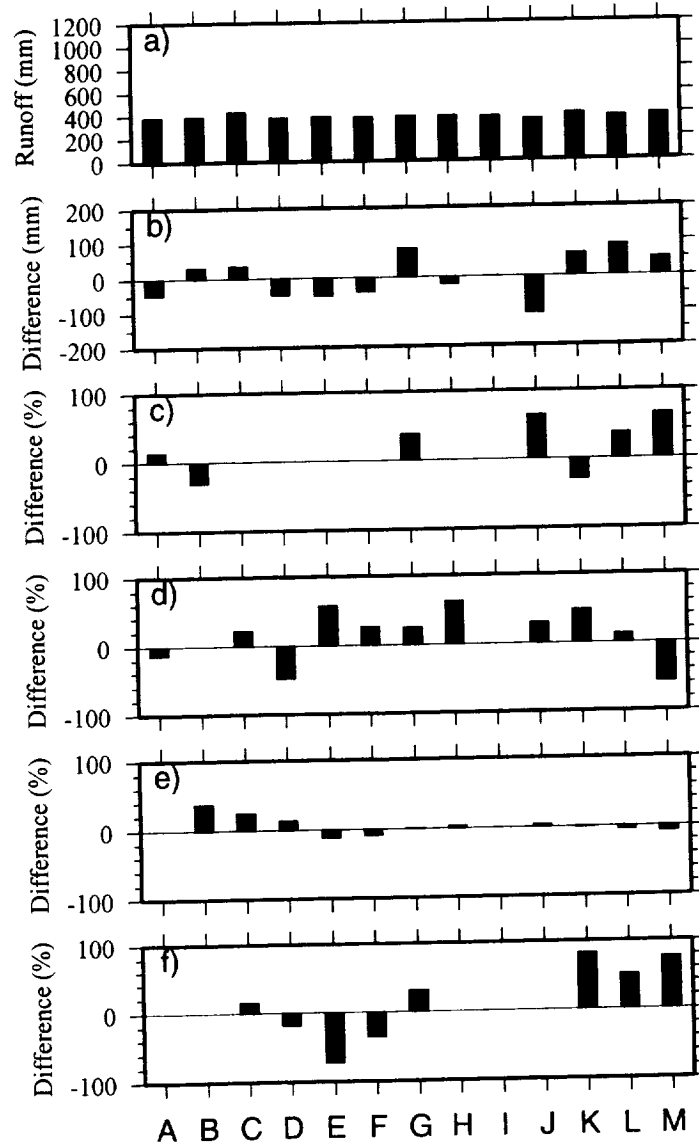


Figure 10: Sensitivity of annual runoff production to bucket model parameters for Region 3. a) Annual runoff with all parameters fixed, b) difference between original and fixed runoff, c) percent difference due to fixed R_a , d) percent difference due to fixed evaporation efficiency, e) percent difference due to fixed albedo and f) percent difference due to fixed snow cover fraction.

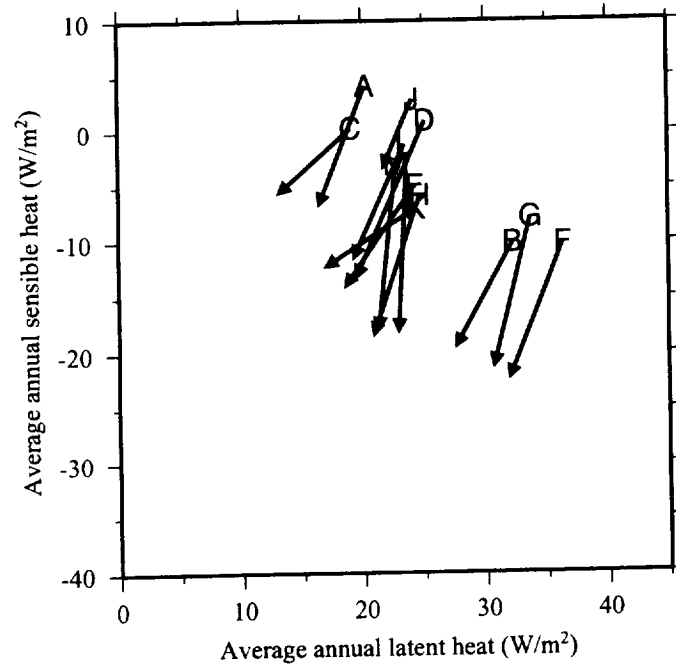


Figure 11: Magnitude and direction of change in average annual sensible and latent heat flux from the original LSSs for Region 2 going between experiment (1) and experiment (2).

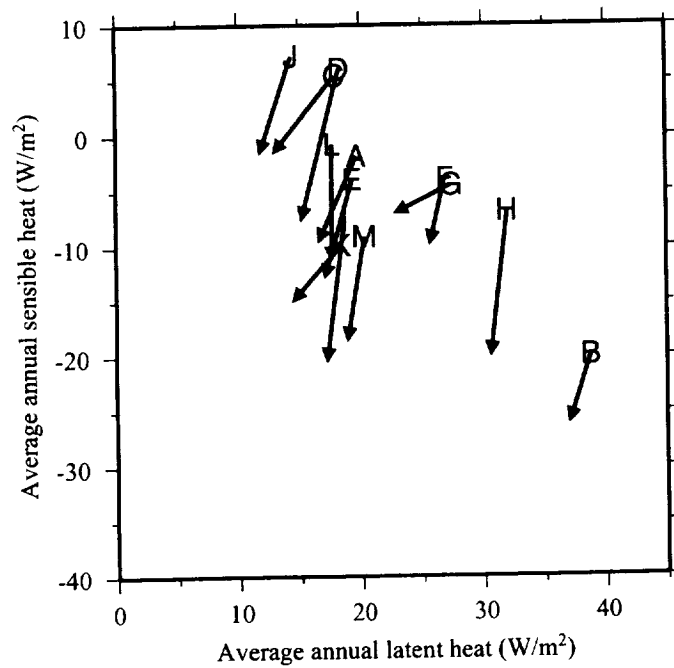


Figure 12: Magnitude and direction of change in average annual sensible and latent heat flux from the SEM for Region 2 going between experiment (1) and experiment (2) forcings and parameters.

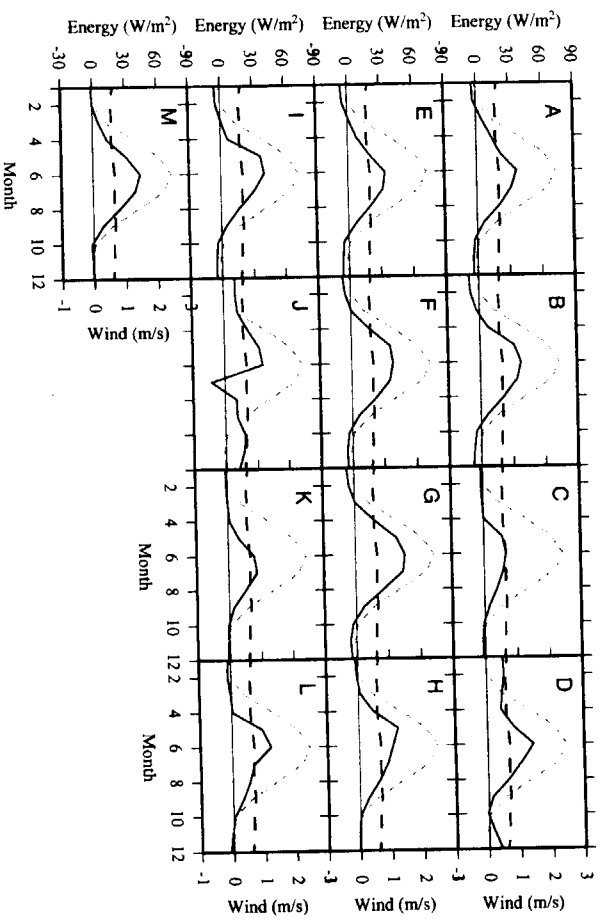
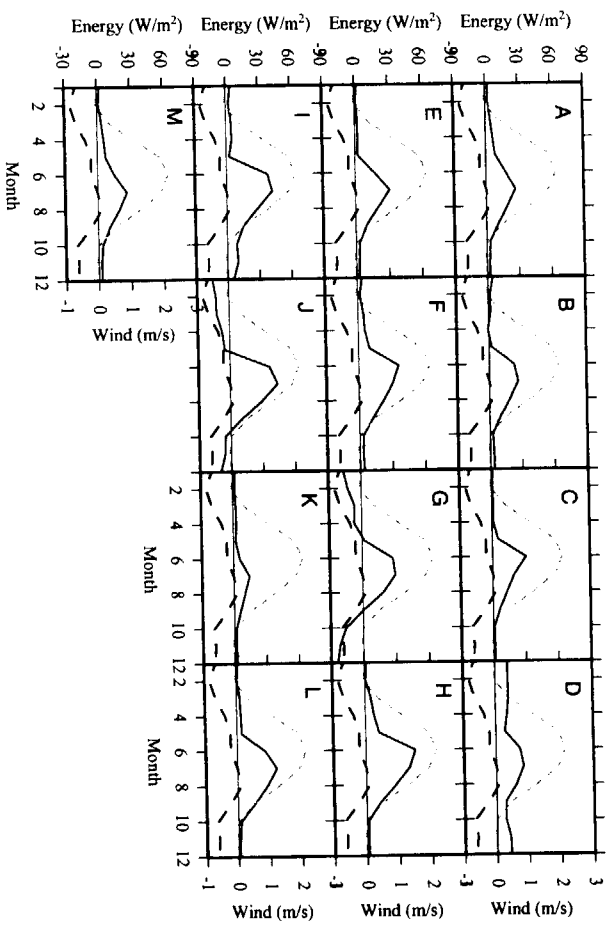


Figure 13: Mean monthly change (experiment 1 – experiment 2) in incoming shortwave (gray dashed), sensible heat (solid black) and wind speed (black dashed) for the LSSs: a) for Region 2 (no overstory) and b) for Region 5 (overstory).

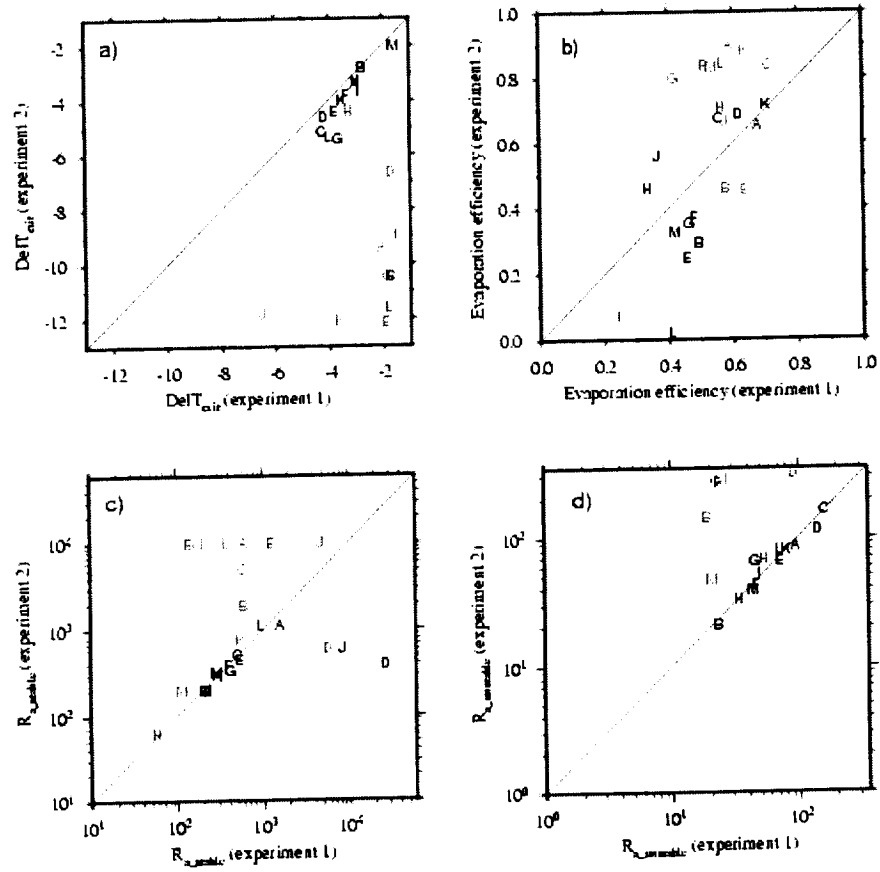


Figure 14: Change in fitted parameters between experiment (1) and (2) for Region 2 (black) and Region 5 (gray): a) ΔT_{crit} , b) B_{ns} , c) r_{a_stable} and d) $r_{a_unstable}$

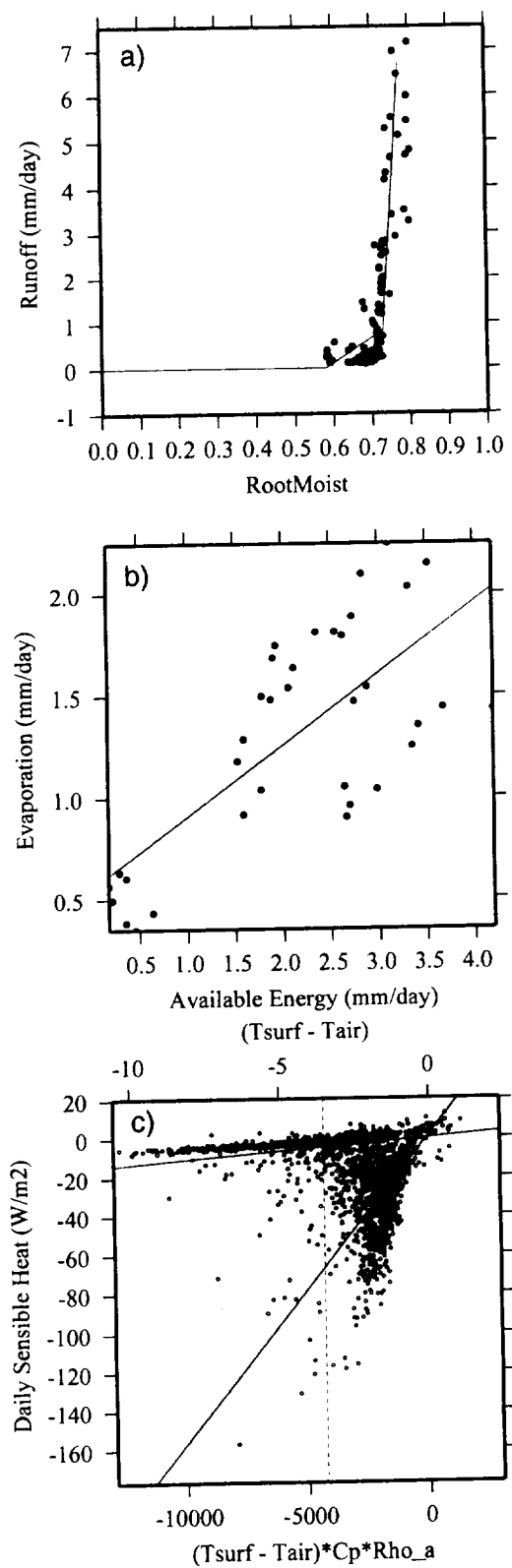


Figure A1: Sample fitting procedure for one LSS: a) Runoff, b) Evaporation and c) aerodynamic resistance.